JOURNAL OF SPACECRAFT AND ROCKETS
Vol. 48, No. 1, January–February 2011

Numerical Analysis of Spacecraft Rocket Plume Impingement Under Lunar Environment

Abhijit Tosh,* Peter A. Liever,† Robert R. Arslanbekov,‡ and Sami D. Habchi§
CFD Research Corporation, Huntsville, Alabama 35805

DOI: 10.2514/1.50813

A numerical investigation is presented for hypersonic rocket exhaust plume flow over lunar surface, a problem offering limited experimental data and significant challenges to computational models in practice. In this paper, examinations on the accuracy of a hybrid continuum-rarefied flow simulation method (unified flow solver) demonstrated close agreements against experimental data for plume shock structures under vacuum conditions and the associated force exerted on the impingement surface. The unified flow modeling approach is then used to resolve the physics of plume expansion under lunar environment, seamless flow transition from continuum to rarefied regime, and the corresponding plume–surface interactions. Analysis of the lander descent action or the plume impingement height revealed significant consequences on the characteristics of supersonic boundary layer, and resulting surface force distributions ranging from near-plume to the far-field observations.

Nomenclature

d_B	=	shock bowl diameter, m
E	=	energy of gaseous medium per unit volume, J/m^3
f	=	velocity distribution function or particle distribution function, m^{-6} s^3
h	=	height from impingement surface, m
I	=	collision integral, m^{-6} s^2
i, j, k	=	direction coordinate indices (dimensionless)
Kn	=	Knudsen number (dimensionless)
p	=	gas pressure, N/m^2
p_j	=	nozzle exit gas pressure, N/m^2
p_s	=	surface pressure, N/m^2
p_∞	=	ambient gas pressure, N/m^2
R	=	physical space, m
R_g	=	specific gas constant, J/kg K
R_n	=	nozzle exit radius, m
r	=	position vector, m
S_ρ	=	breakdown parameter (dimensionless)
T, T_{ref}	=	gas temperature, reference temperature, K
t	=	time, s
u, v, w	=	velocities along x, y, z directions, m/s
V_{ref}	=	reference thermal velocity, m/s
x, y, z	=	direction coordinates, m
γ	=	ratio of specific heats of gas
Δ	=	shock standoff distance, m
ξ, ξ_x	=	velocity vector, velocity in x direction, m/s
ρ	=	gas density, kg/m^3
τ, τ_m	=	surface shear stress, maximum stress, N/m^2
ψ	=	collision invariant (dimensionless)

Received 18 May 2010; revision received 10 September 2010; accepted for publication 22 September 2010.

*Senior Engineer, Aeromechanics, 215 Wynn Drive, Suite 501; tosh.abhijit@gmail.com. Senior Member AIAA.

†Technical Fellow, Aeromechanics, 215 Wynn Drive, Suite 501. Senior Member AIAA.

‡Senior Principal Scientist, Aerospace and Defense, 215 Wynn Drive, Suite 501.

§Vice President, Aerospace and Defense, 215 Wynn Drive, Suite 501. Senior Member AIAA.

I. Introduction

A LUNAR spacecraft lands with a gradual powered-descent approach [1], its thruster rocket nozzle or multiple engine clusters being directed towards the surface of the moon. Because of the absence of an atmosphere, the lunar environment allows the hypersonic rocket plume to expand from a high-pressure continuum flow to the external vacuum surroundings, where the gas flow undergoes a transition to rarefied condition. The rarefied plume then impinges on the lunar surface developing a bowl-shaped standoff shock [2]. The flow recompresses to a near-continuum stagnation region, followed by a supersonic boundary layer flow outward across the lunar surface. This supersonic boundary layer expands again to a rarefied flow into vacuum. The static pressure exerted on the lunar surface, is maximum beneath the engine that descends quickly in the radial direction. While, the dynamic pressure reaches a maxima at a certain radial location imposing a maximum surface shear stress. Because of transfer of radial momentum from the flow to the loosely packed blanket of soil [3], the lunar surface endures a viscous erosion process [4]. Soil debris being readily lofted from the surface is then dramatically accelerated to the order of lunar escape velocity level ($\approx$2.37 km/s) [5].

Present understanding of the lunar plume impingement effects is based on a combination of Apollo astronaut observations [6], measured Surveyor 3 impact and erosion effects [7], analysis of Apollo landing video imagery from inside the lander window, post-landing photographs [8,9], and terrestrial experiments with limited realism [10–16]. For the Apollo landings, viscous erosion of the surface layer of dust and sand-sized particles just a few centimeters thick has been identified as the main mechanism for soil erosion and loss of visibility [17]. The lack of any lunar atmosphere and resulting drag forces allow the debris particles to travel unimpeded along ballistic trajectories over considerable distances. The most serious dust environment occur during rocket assisted launch and landing operations. The Apollo 12 Lunar Module landing 155 m away from the Surveyor 3 spacecraft provided an indication of the risks encountered by colanding critical hardware. The surfaces of the Surveyor 3 had been observed to be sandblasted by a high-speed shower of dust particles during the landing. The liberation of debris caused by spacecraft landing on the dusty lunar soil threatens to be one of the highest risks facing lunar exploration system architectures [18] through visual obscuration, false instrument readings, clogging, and abrasion. The effects of the plume induced debris transport thus has a fundamental impact on the design of lunar landing craft, landing operations procedures, and requirements for spatial separation of landing and habitation areas for lunar exploration.

Because of limitations in conducting terrestrial experiments on such phenomena, future generation space exploration systems will mostly rely on the predictions of appropriate physics models. Available analytical method for predicting the observed soil erosion rates is based on the theory of viscous erosion mechanisms for lunar dust, initially developed by Roberts [19]. Roberts' method was derived from first principles, assuming that erosion is a shearing process occurring only when the gas-phase shear stress is larger than the soil shear strength. His method then assumes that the excess shear stress in the gas boundary layer is exactly transformed into momentum of the eroding soil particles. However, in reality the erosion mechanism is hardly dependent on the bulk shearing of the soil, since debris particles are individually carried away without being sheared across the surface with horizontal friction beneath the normal stress. Further, the model does not account for the fundamentally different lunar flow conditions, and becomes invalid below a critical nozzle distance from the ground. The limitations of Roberts' theory in the predictions of soil erosion were drawn through comparison against experiments by Hutton [20]. Metzger et al. [21,22] have scrutinized the assumptions made in Roberts' model and made significant improvements.

The complex nature of plume–surface interactions occurring across a mixture of continuum and rarefied flow need to be characterized first before understanding and relating it to the soil erosion mechanism. The peculiar flow conditions offer enormous challenges to computational modeling approaches as well. Application of a continuum Navier–Stokes flow solver in the near-vacuum outer plume regions will be simply inaccurate. The currently prevailing numerical approach of simulating this kind of mixed flow is the particle model-based direct simulation Monte Carlo (DSMC) method. The DSMC method [23–25] is based on statistical sampling of particle motion and collisions. The typical coupling technique of mixed rarefied-continuum flow is to identify a so-called breakdown surface where the continuum assumption starts to fail [26,27]. The resulting subdomains are then solved separately with DSMC and Navier–Stokes flow solvers communicating at the breakdown surface interface. A number of researchers [28–32] have demonstrated the hybrid continuum-rarefied simulations through domain decomposition using the DSMC technique for the kinetic domain.

In contrast to the hybrid Navier–Stokes/DSMC methods, this paper presents simulations using a recently developed hybrid continuum-rarefied flow solver [33] known as the unified flow solver (UFS), for more efficient description of the physics of lunar plume impingement. The features of UFS approach are suitably used with its capability of computing mixed continuum-rarefied-vacuum flows across the flow regimes from low subsonic to supersonic/hypersonic in a single simulation without the soil erosion physics.

II. Numerical Method

The work presented in this paper uses the combination of gas kinetic Euler and Boltzmann transport equations in the UFS, a hybrid continuum-rarefied computational fluid dynamics method that has emerged as a unique alternative to the hybrid Navier–Stokes/DSMC solution approaches. Using the adaptive Cartesian mesh refinement (open source) framework of the Gerris flow solver [34], the UFS has been developed for efficient hybrid simulations across the spectrum of rarefied, transitional and continuum flows by coupling a Boltzmann kinetic solver with gas kinetics-based continuum flow solvers. Description of the computational architecture is briefly presented here. Details of UFS numerical methods can be found in Kolobov et al. [35,36].

The kinetic Euler scheme of UFS continuum equations is based on the equilibrium flux method developed by Pullin [37]:

$$\frac{\partial Y}{\partial t}+\frac{\partial F}{\partial x}+\frac{\partial G}{\partial y}+\frac{\partial H}{\partial z}=0$$

where

$$\begin{aligned} Y &= \{\rho, \rho u, \rho v, \rho w, E\} \\ F &= \{\rho u, p/2+\rho u^2, \rho vu, \rho uw, u(E+p)\} \\ G &= \{\rho v, \rho uv, p/2+\rho v^2, \rho vw, v(E+p)\} \\ H &= \{\rho w, \rho uw, \rho vw, p/2+\rho w^2, w(E+p)\} \end{aligned} \tag{2}$$

where ρ is the density, u, v, w are the velocities along x, y, z coordinates, p is the pressure, and E is the energy of the gaseous medium. Here, the governing equations are discretized using finite volume technique and fluxes at the computational cell faces are obtained from the integrals of the product of velocity distribution functions (VDF) and collision invariants [38]:

$$\frac{Y^{n+1}_{ijk}-Y^{n}_{ijk}}{\Delta t}=-\left(\frac{F^{n}_{i+1/2,j,k}-F^{n}_{i-1/2,j,k}}{\Delta x}+\frac{G^{n}_{i,j+1/2,k}-G^{n}_{i,j-1/2,k}}{\Delta y}+\frac{H^{n}_{i,j,k+1/2}-H^{n}_{i,j,k-1/2}}{\Delta z}\right) \tag{3}$$

where Y^{n}_{ijk} is the cell averaged value of Y at time t^n and $F^{n}_{i+1/2,j,k}$, $G^{n}_{i,j+1/2,k}$ and $H^{n}_{i,j,k+1/2}$ are the fluxes on cell faces along x, y, and z. The VDF are calculated as

$$F^{n}_{i+1/2,j,k}=\frac{1}{\Delta t}\int_{t^n}^{t^{n+1}}\int_{R^3}\psi\xi_x f(x_{i+1/2},t,\xi)\,\mathrm{d}\xi\,\mathrm{d}t \tag{4}$$

where ψ is the collision invariant and f is the VDF at the cell faces. The fluxes $G^{n}_{i,j+1/2,k}$ and $H^{n}_{i,j,k+1/2}$ are computed in a similar way.

The rarefied flow regime in UFS is resolved by the particle distribution function in a six-dimensional phase space evolved from the Boltzmann transport equation [39]. Introduction of a Cartesian mesh velocity grid space in the numerical scheme reduces the equation to a system of linear hyperbolic transport equations in physical space with a nonlinear source term for the collision integral (I):

$$\frac{\partial f}{\partial t}+\nabla_r\cdot(\xi f)=I(f,f) \tag{5}$$

where $f(t,r,\xi)$ is the particle distribution function, ξ is the velocity vector, r is the position vector in physical space and t is the time.

Coupling between the continuum and rarefied solvers in UFS is implemented through the corresponding VDF at the breakdown interface. The interface is identified by a threshold value of the breakdown criteria (S_ρ), a function of the local Knudsen number (Kn) and the gradient of mass density:

$$S_\rho=Kn\frac{1}{\rho}|\nabla\rho| \tag{6}$$

In the UFS numerical technique, the use of the first-principle based Boltzmann transport equation offers significant advantages. The nonstatistical Boltzmann transport equation in the particle kinetic regime allows application of solver techniques for both the continuum and kinetic models with nearly seamless coupling of the continuum and kinetic domains. The accuracy and robustness advantages of the Boltzmann solution approach are particularly striking for low speed rarefied flows. Moreover, this hybrid method provides significant time savings by limiting kinetic scale solutions only to regions where they are needed [36]. Since the CPU time requirement for the continuum solver is more than 1 order of magnitude lower than for the Boltzmann solver, using an intelligent domain decomposition method this hybrid scheme provides excellent numerical stability and also substantial speed-up of the simulations at the same time. Evaluation of UFS predictive capability and its advantages in comparison against the DSMC method have been presented by Josyula et al. [40] for a hypersonic nozzle plume flow.

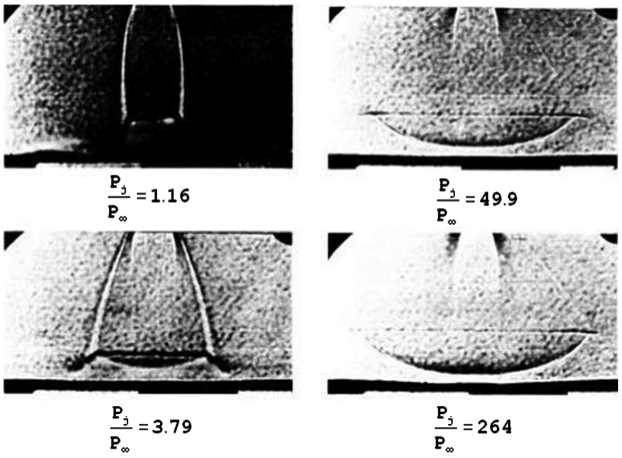

Fig. 1 Experimental shadowgraphs of Land and Clark [2].

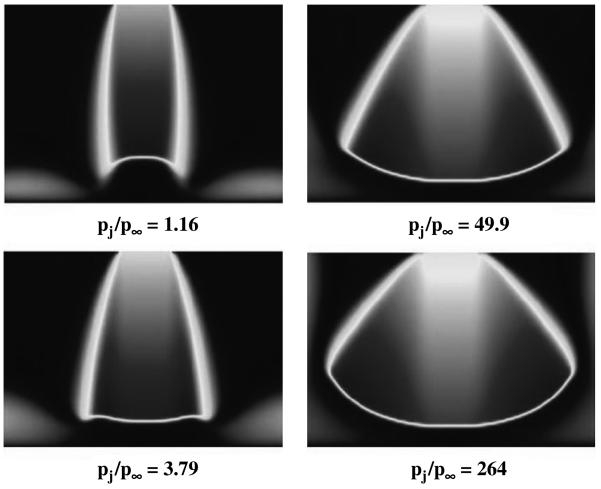

Fig. 2 UFS Mach contours under varying nozzle exit-to-ambient pressure ratios.

III. Results and Discussions

In this numerical study, the accuracy of UFS predictions is first validated against experimentally conducted plume impingement tests under variable vacuum conditions. The plume flow characteristics under lunar environment are then investigated to characterize the effect of spacecraft proximity to the lunar surface.

A. UFS Validation for Plume Impingement Under Vacuum

The accuracy of UFS predictions using Euler gas kinetics scheme (with first order accuracy) and the Boltzmann transport equation was examined by simulating a radially symmetric supersonic plume exhausting from a nozzle into near-vacuum and impinging on a surface. Experimental tests were conducted by Land and Clark [2] for flow impingement of nitrogen gas on a flat surface under a wide range of nozzle exit-to-ambient pressure ratios ($p_j/p_\infty = 0$ to 270) and various nozzle distances from the surface. The conical nozzle (15° half-cone) with an exit diameter of $5/8$ inch employed in these tests

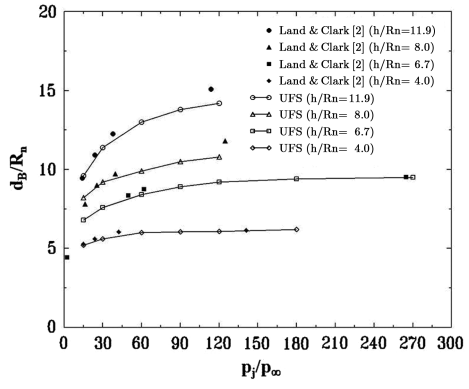

Fig. 3 Variation of shock bowl diameter with nozzle exit-to-ambient pressure ratio.

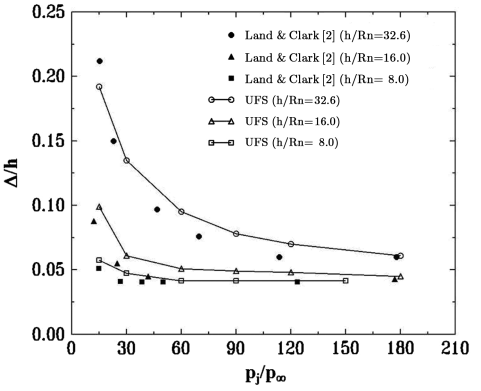

Fig. 4 Variation of shock standoff distance with nozzle exit-to-ambient pressure ratio.

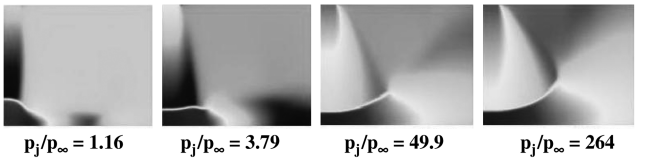

Fig. 5 Effect on pressure due to nozzle exit-to-ambient pressure ratio.

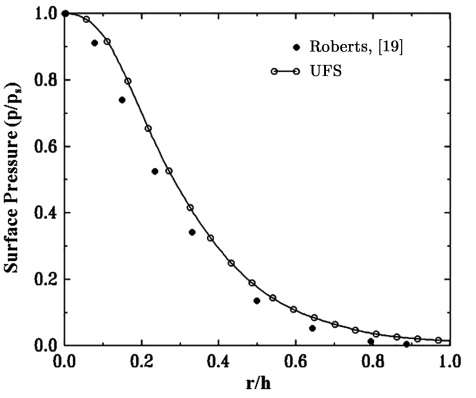

Fig. 6 Plume impingement surface pressure distribution.

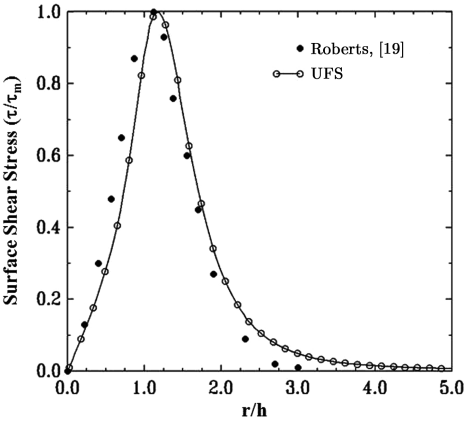

Fig. 7 Plume impingement surface shear stress distribution.

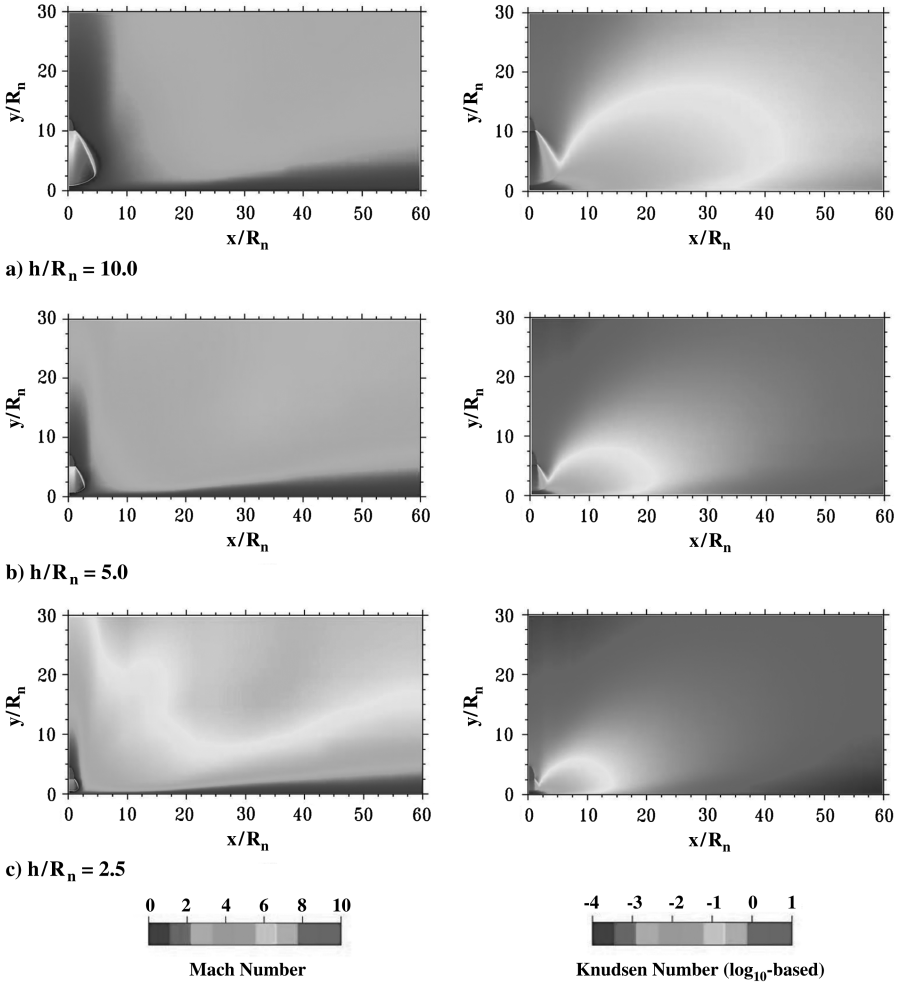

Fig. 8 UFS contours of Mach (left) and Knudsen (right) numbers.

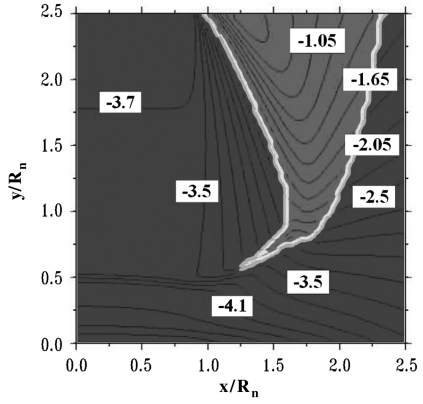

Fig. 9 Hybrid domain decomposition ($h/R_n = 2.5$ with $\log_{10}$-based Knudsen number).

was designed [12] for an exit Mach number of 5.0. The experimental results provided both qualitative and quantitative descriptions of the nature of plume flow field. Fixed flow conditions were imposed for UFS computations at the nozzle exit boundary, with axisymmetric condition on the plane of plume centerline. The computational domain was extended to 30 and 60 times the nozzle exit radius (R_n) in the plume normal and radial directions, respectively. The boundaries in these directions were set to free exit conditions for the gas-phase and diffuse reflection conditions on the solid impingement surface using the Boltzmann solver. The mass density gradient and local Knudsen number based continuum-rarefied breakdown criteria for hybrid domain decomposition was used with a threshold value of 0.025. In UFS simulations, both internal (rotational and vibrational) and translational energies were considered for a single species diatomic gas.

As presented in the experimental shadowgraphs in Fig. 1, four different nozzle exit-to-ambient pressure ratios, $p_j/p_\infty = 1.16$,

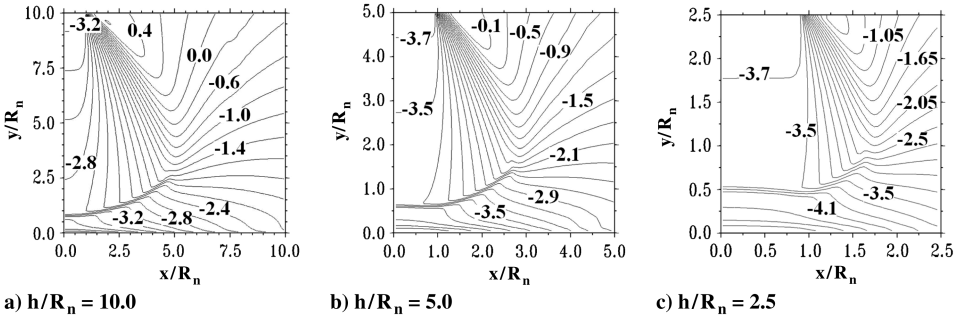

Fig. 10 Transition of Knudsen number ($\log_{10}$-based).

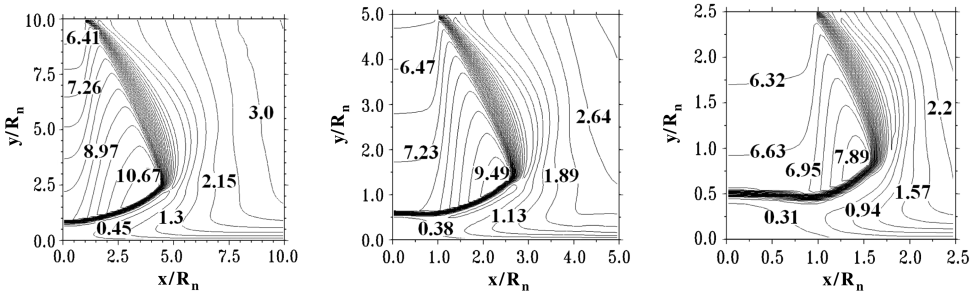

a) $h/R_n = 10.0$ b) $h/R_n = 5.0$ c) $h/R_n = 2.5$

Fig. 11 Transition of Mach number.

3.79, 49.9 and 264.0 were selected for simulations for an impingement height-to-nozzle radius ratio (h/R_n) of 6.7. The contours of Mach number obtained from UFS simulations in Fig. 2 presents a qualitative comparison against the shadowgraphs of the experiments. The Mach contours (images mirrored about the axis of symmetry) illustrate the dramatic effect on plume expansion, while the shock standoff distance under the curved sonic lines can be observed to decrease upon increasing the pressure ratio. The presence of an

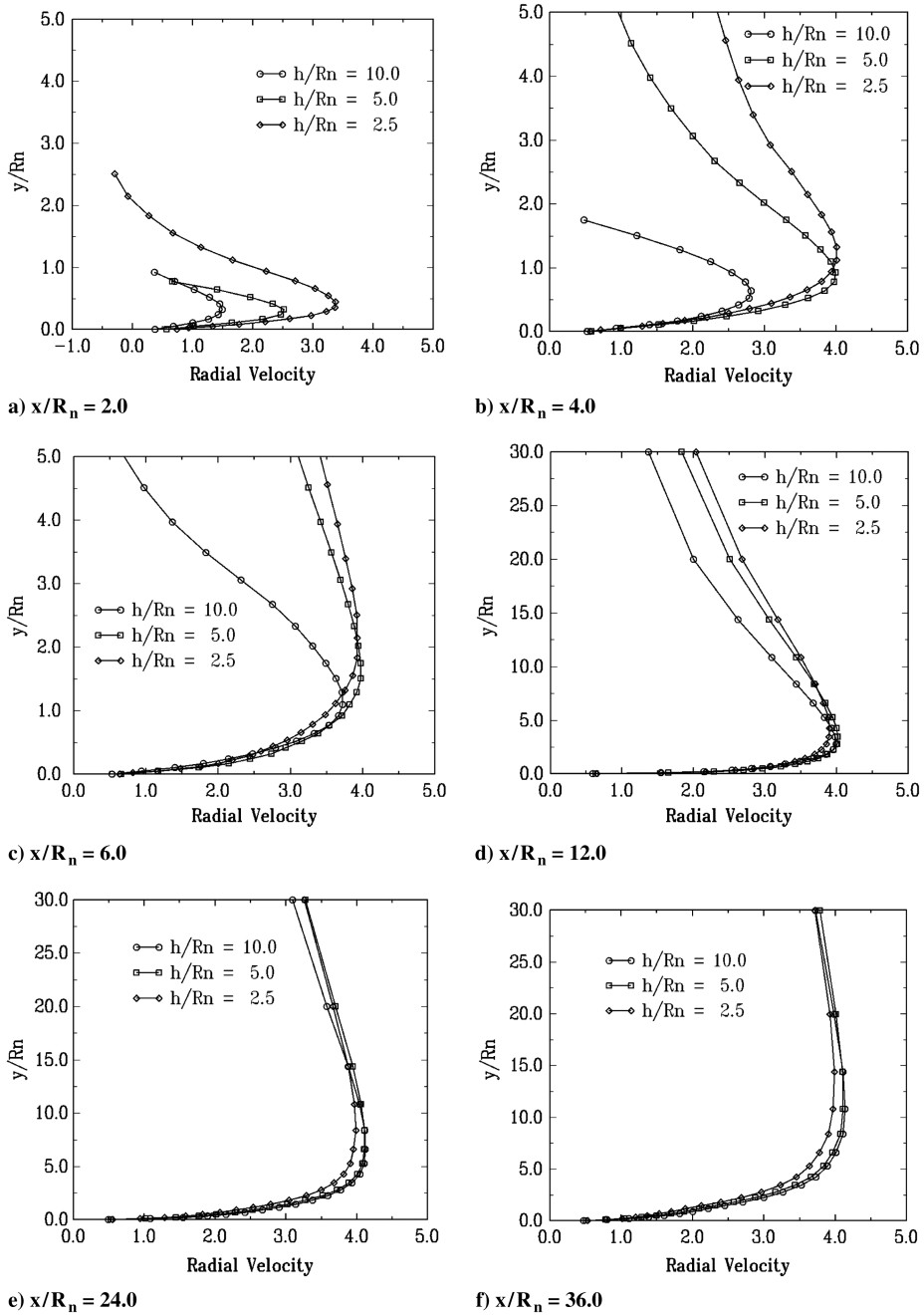

a) $x/R_n = 2.0$ b) $x/R_n = 4.0$

c) $x/R_n = 6.0$ d) $x/R_n = 12.0$

e) $x/R_n = 24.0$ f) $x/R_n = 36.0$

Fig. 12 Radial velocity profiles.

inflection point in the standoff shock at the lower pressure levels and its disappearance for the high expansion ratios is well-resolved with UFS. As observed in the experiments also [2,12], these inflection points are distinctive under lower pressure ratios due to the expansion waves of the standoff shock which diminish with plume expansion under increasing vacuum conditions or at higher pressure ratios.

Quantitative assessment of UFS results against experimental data was performed through measurements of the normal shock bowl diameter and shock standoff distance under various nozzle exit-to-ambient pressure ratios and impingement heights. For this study, simulations were mostly carried out for $p_j/p_\infty = 15, 30, 60, 90, 120,$ and 180 in order to consider the available experimental data range. As evident in the experimental shadowgraphs and UFS Mach contours, the shock bowl diameter is predicted to gradually expand upon increasing the pressure ratio, ultimately reaching a near constant value. A similar behavior is predicted with a decrease in the shock height. The maximum Prandtl–Mayer expansion angle 76.95° at Mach number 5.0 compares well with UFS predictions of 77.1° of the asymptotic bowl diameters. UFS predictions of the normal shock bowl diameters (d_B/R_n) for impingement height-to-nozzle radius ratios $h/R_n = 4.0$, 6.7, 8.0 and 11.9 shown in Fig. 3 demonstrate close agreement with the experiments for all impingement heights. Results of the normal shock standoff distances (Δ/h), depicted in Fig. 4 also follow the trends of experimental profiles for $h/R_n = 8.0$, 16.0 and 32.6. The total number of continuum/Boltzmann cells were 10,629/4718 for the case of $h/R_n = 8.0$ at $p_j/p_\infty = 90$ with $24 \times 24 \times 12$ velocity grid size for the Boltzmann solver. The corresponding simulation runtime was 4.7 h on five cluster nodes using one Advanced Micro Devices (AMD) processor core per node (64 bit, 2.2 GHz speed, 2056 MB total memory).

The contours of the nondimensional pressure field ($\log_{10}$-based) shown in Fig. 5 for $h/R_n = 6.7$, illustrate the characteristics of plume–surface interaction under varying exit-to-ambient pressure ratios. A strong effect of plume impingement on the surface is revealed with a high-pressure field underneath the bowl shocks that rapidly diminishes along the radial direction on the surface (r/h). This flow behavior and the surface forces exerted are confirmed well by the UFS representation of the surface pressure distribution (p/p_s) in Fig. 6 and surface shear stress distribution (τ/τ_m) in Fig. 7 for the case of $h/R_n = 8.0$ at $p_j/p_\infty = 90$, in agreement with the theory presented by Roberts [19].

The hypersonic plume–surface interaction problem presented preceding is much like the lunar landing scenario. Since the lunar environment is difficult to recreate in terrestrial experiments due to the high expense of lunar stimulant and practicality of hypersonic plume expansion in vacuum chamber, the fundamental physics models in UFS can be relied upon for simulations of the lunar gas dynamics and surface interactions. The assessment of UFS results conducted in comparison with experimental tests shows the capability of accurate predictions of such flow characteristics.

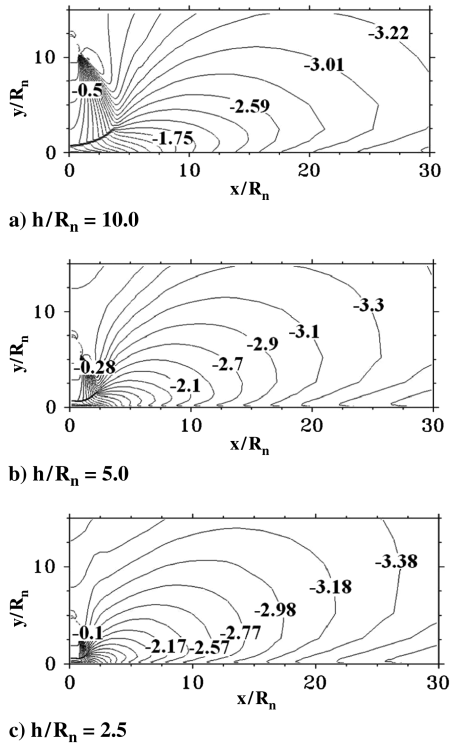

Fig. 13 Contours of flow density field ($\log_{10}$-based).

B. Plume Impingement Analysis Under Lunar Environment

The objectives of these studies are a) to investigate the physics of a radially symmetric hypersonic plume flow effects under lunar environment, b) to resolve smooth transition from highly continuum to extremely rarefied flow conditions, and c) to predict the distribution of forces on the impingement surface with variation of nozzle height. A detailed description of this rocket exhaust plume–surface flow physics is essential for its effect on the viscous lunar soil erosion rate and consequent dust transport in the surrounding. In these numerical experiments, UFS hybrid simulations with a breakdown threshold value of 0.025 were performed to achieve steady-state results with three stages of nozzle radius-to-height ratios ($h/R_n = 10.0$, 5.0, 2.5) above a flat impingement surface. The rectangular computational domain spanned $60 \times R_n$ in the radial and $30 \times R_n$ in the plume normal directions.

An inflow boundary condition was used to create the Apollo lunar excursion module (LEM) engine plume flow originating from the nozzle exit surface. The nozzle exit profile of the LEM engine exhaust flow at the 30% engine power level [1] was used for the plume inflow boundary condition with axisymmetric conditions along the plume centerline. The resulting nozzle exit Mach = 6.0 and Knudsen number (Kn) $= 1.6 \times 10^{-4}$, represented full continuum flow for the gas kinetics-based Euler simulations (first order accurate) in UFS assuming an inviscid ideal gas flow. The diffuse reflection condition on the solid impingement surface using the Boltzmann solver was imposed along the radial direction and the far-field condition was set to $p_\infty = 8 \times 10^{-9}$ Torr (ambient to nozzle exit pressure ratio of 2.133×10^{-8}). This ambient pressure was selected based on Apollo 12 lunar atmosphere assessment by West et al. [18]. Both internal (rotational and vibrational) and translational energies were considered for a single species diatomic gas. Adequate computational cells were used for high resolution of the shock structures. The total number of continuum and Boltzmann cells used for these simulations were 6859/5619, 9853/8886 and 11,419/11,290 for the cases $h/R_n = 2.5$, 5.0 and 10.0, respectively, and used $24 \times 24 \times 12$ velocity grid size for the Boltzmann solver. The corresponding simulation runtimes were 10.6, 16.5 and 21 h on five cluster nodes using one AMD processor core per node (64 bit, 2.2 GHz speed, 2056 MB total memory).

1. *Flow Mach and Knudsen Numbers*

The UFS flow contours of Mach and Knudsen numbers are shown in Fig. 8. At $h/R_n = 10.0$, the plume is observed to expand under the lunar rarefied environment resulting a curved bowl shock standoff above the surface. As the impingement height decreases, the overall plume expansion volume is observed to be effectively reduced as the bowl diameter (d_B/R_n) of the jet boundary decreases in the order 9.7, 5.6 and 3.6 with the nozzle descent and the normal shock sonic line gets flattened due to surface proximity. The contours of the Knudsen number ($\log_{10}$-based Kn) show the distinctive regions of near-plume continuum flow (low Kn, dark), the off-plume rarefied flow (high Kn, bright) and the seamless intermediate flow transition resolved by UFS. The hybrid domain decomposition method of UFS in Fig. 9 shows the transition of the $\log_{10}$-based Kn with the rarefied (bright) and continuum (dark) regions for $h/R_n = 2.5$.

The effect of impingement height on the transition of flow Knudsen number (Kn) and the flow Mach number are represented in Figs. 10 and 11. The contour lines ($\log_{10}$-based numbers) confirm

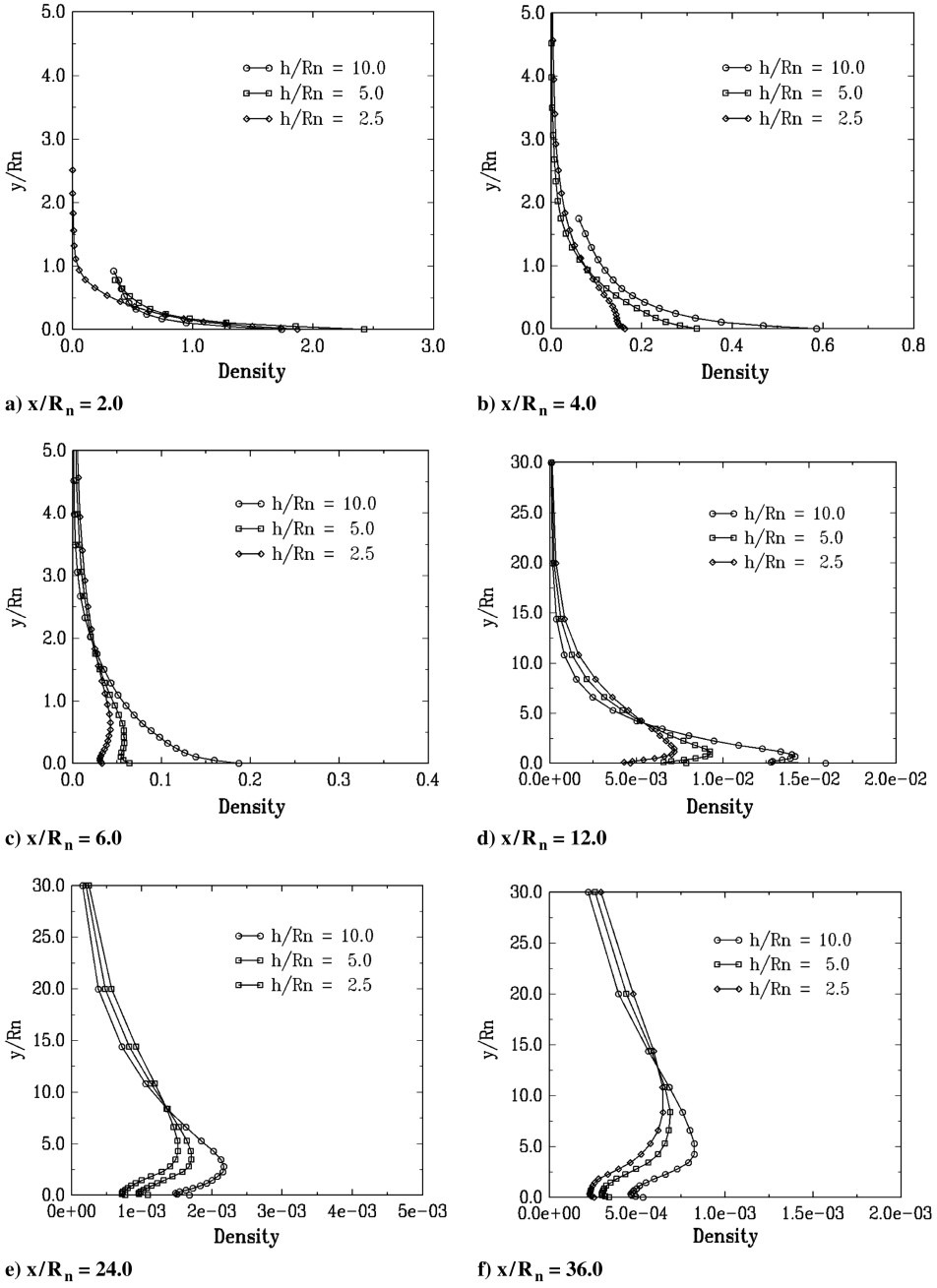

Fig. 14 Density profiles.

that in the vicinity of the plume, the Knudsen number is of the order of 10^{-4} (nozzle exit), which undergoes a smooth transition to the rarefied condition by a gradual rise to the order of $0.2 < Kn < 2.5$ for $2.5 < h/R_n < 10.0$, in the plume normal direction. The nozzle height effect on the flow transition in the far-field is also evident from these contours (Figs. 8 and 10). The low Knudsen number (continuum) zone is compressed by effect of the nozzle descent. However, due to stronger impingement effect during the descent action, the continuum flow direction is reflected more toward the vertical direction, as shown by elevated values of the Knudsen number at lower heights. The flow Mach number contours in Fig. 11 shows the reduction in shock bowl diameter lowering the nozzle height and the corresponding structure of the sonic line. The Mach levels inside the plume steadily increases from the nozzle exit plane to the sonic line, while flow transition occurs beneath the plume standoff from subsonic to supersonic range along the radial direction.

The contours and profiles of nondimensional radial velocity, density, and pressure flow fields along the plume normal direction ($0.0 < y/R_n < 30.0$) were examined at various radial locations (x/R_n) ranging from near-plume to far-field locations. The flowfield monitor points in the UFS simulations were clustered near the solid surface in order to identify variations of the flow properties and subsequent physical gradients in the supersonic surface boundary layer.

2. *Flow Radial Velocity*

The behavior of the radial velocity in the supersonic surface flow is shown in Fig. 12. The velocity field in UFS is normalized to the thermal velocity $V_{\text{ref}} = \sqrt{(2R_g T_{\text{ref}})}$, where $T_{\text{ref}} = 500$ K was considered in these simulations. Profiles of the near-plume continuum region ($x/R_n = 2.0$, 4.0 and 6.0) show presence of significant gradients in the surface normal direction ($0.0 < y/R_n < 1.0$). Under lower nozzle heights for a certain y/R_n, higher magnitudes and variations of radial velocity are detected very close to the impingement surface. These gradients diminish as the flow proceeds radially outward. The radial velocities for all impingement heights tend to merge at large distances as the flow regime becomes rarefied. Evidence of this strong gradient in the supersonic radial flow

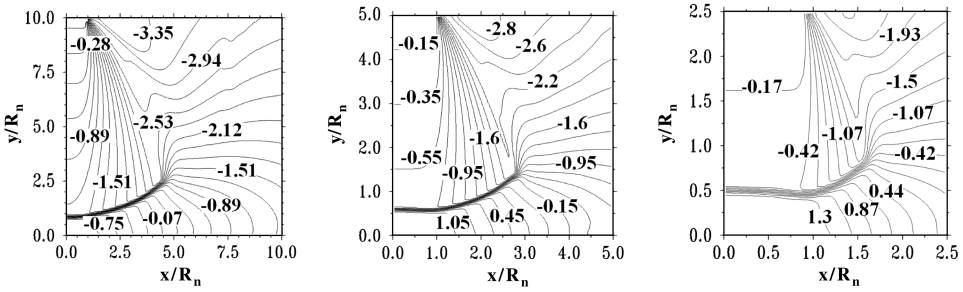

a) $h/R_n = 10.0$ **b) $h/R_n = 5.0$** **c) $h/R_n = 2.5$**

Fig. 15 Contours of flow pressure field ($\log_{10}$-based).

justifies a functional relation with the surface shear force acting in the near-plume region. It is to be noted that during the lander engine shutdown stage under subsonic flow regime, a boundary layer transition from laminar to fully turbulent regime is likely to occur depending on the nearness of the nozzle height to the surface, the roughness scales of the lunar regolith and entrained dust particles [41]. This viscous boundary layer has a critical impact on the lunar soil erosion mechanism caused by frictional stress.

3. Flow Density Field

The flow density contours ($\log_{10}$-based) under various nozzle heights are illustrated in Fig. 13. It can be observed that the density at the near-plume exhaust is of the order of the nozzle exit condition ($\rho = 1.0$) that rapidly decreases to negligibly small magnitudes both vertically and radially outward in the lunar environment. The contour levels illustrate that the overall influence of continuum flow region in the plume flowfield environment reduces upon lander descent. Thus once eroded due to increasing impingement pressure and resulting shear forces, the lunar soil debris will be easily lofted from the surface and greatly accelerated in the surrounding without any drag force offered by the gas. It can also be envisaged that at lower engine heights, the dust particles trajectories will have more vertical orientation due to flow reflection.

The density profiles at various radial distances are plotted in Fig. 14. In these plots, it is confirmed that the near-plume density undergoes a rapid transition from the order of the plume origin condition merging smoothly to a low gas density of the lunar environment. Because of predominance of continuum flow close to the surface, the density field is not much affected by the nozzle height variation in the near-plume region ($x/R_n = 2.0$). However, due to different extents of flow transition region induced by the impingement height, the profiles gradually depart from each other with small vertical gradients along the radial direction. The fluid density sharply decreases along large radial distances due to rarefaction of the gas under lunar vacuum. The transition from highly continuum to highly rarefied regime and the surface flow characteristics are clearly notable in these figures.

4. Flow Pressure Field

The resulting fluid pressure under the plume at various nozzle distances and the corresponding force distribution on the impingement surface are presented in Figs. 15 and 16. The surface pressure and shear stress in Fig. 16 are normalized by $0.5\rho u^2$ based on nozzle exit conditions $\rho = 1.0$ and $u = \text{Mach}\sqrt{(\gamma T/2)}$ with $T = 1.0$ (T being normalized to the reference temperature T_{ref} in UFS). The contours of the $\log_{10}$-based flow pressure in Fig. 15 display a direct effect of the nozzle height on the plume near-field flow. It is revealed in Fig. 16a, that the magnitude of maximum surface pressure or the normal force exerted at the plume centerline increases approximately by a factor of two due to decreasing nozzle height by the same factor. The influence of shock bowl diameter is also notable both in Figs. 15 and 16, where the surface forces have reduced effect of the plume in the radial direction (x/R_n) with height descent. A transfer mechanism of plume normal forces to the radial direction can be explained by the peaks of surface shear stress at a certain radial location in Fig. 16b.

This phenomenon occurs when the radial distance crosses the flat region of the standoff shock ($r/R_n \approx 1.0$), where the sonic line curves to form the bowl shape. The sharp decline in the pressure peaks are consequently balanced by rise in the surface tangential forces. This typical behavior of the surface shear forces has been explained by Roberts [19] through theoretical formulations of shear stress distribution along the radial direction.

The characteristics of near-plume and far-field flow pressures are presented in Fig. 17. The near-plume profiles in Fig. 17 portray a direct influence of the plume impingement height. As seen in Fig. 16, these plots also reflect that higher nozzle heights will impose larger area of the pressure distribution on the surface, even though the magnitude of surface pressure at the plume center is roughly doubled with decreasing height. This is evident with declining pressure magnitudes with the height for all radial locations. However, the pressure gradients along the vertical direction are significantly large for higher nozzle heights, dropping quickly into the rarefied environment. As observed in the density profiles, the plots of flow pressure in Fig. 17 also indicate the effect of flow transition from

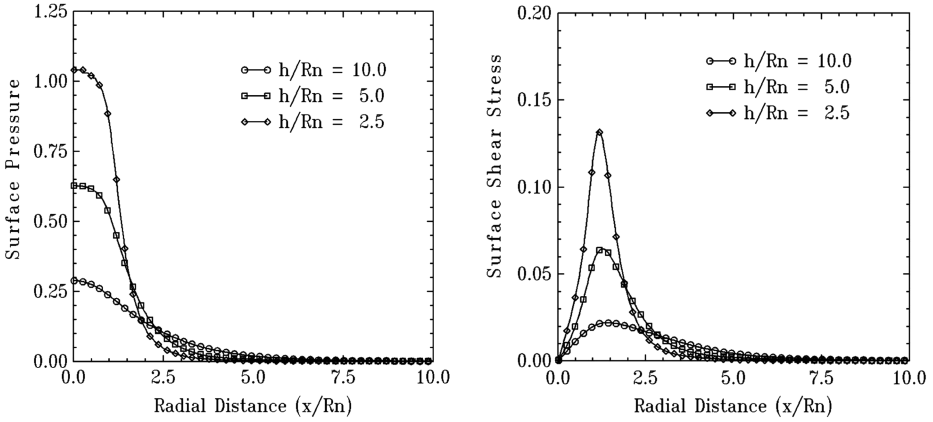

a) Surface pressure **b) Surface shear stress**

Fig. 16 Impingement surface forces.

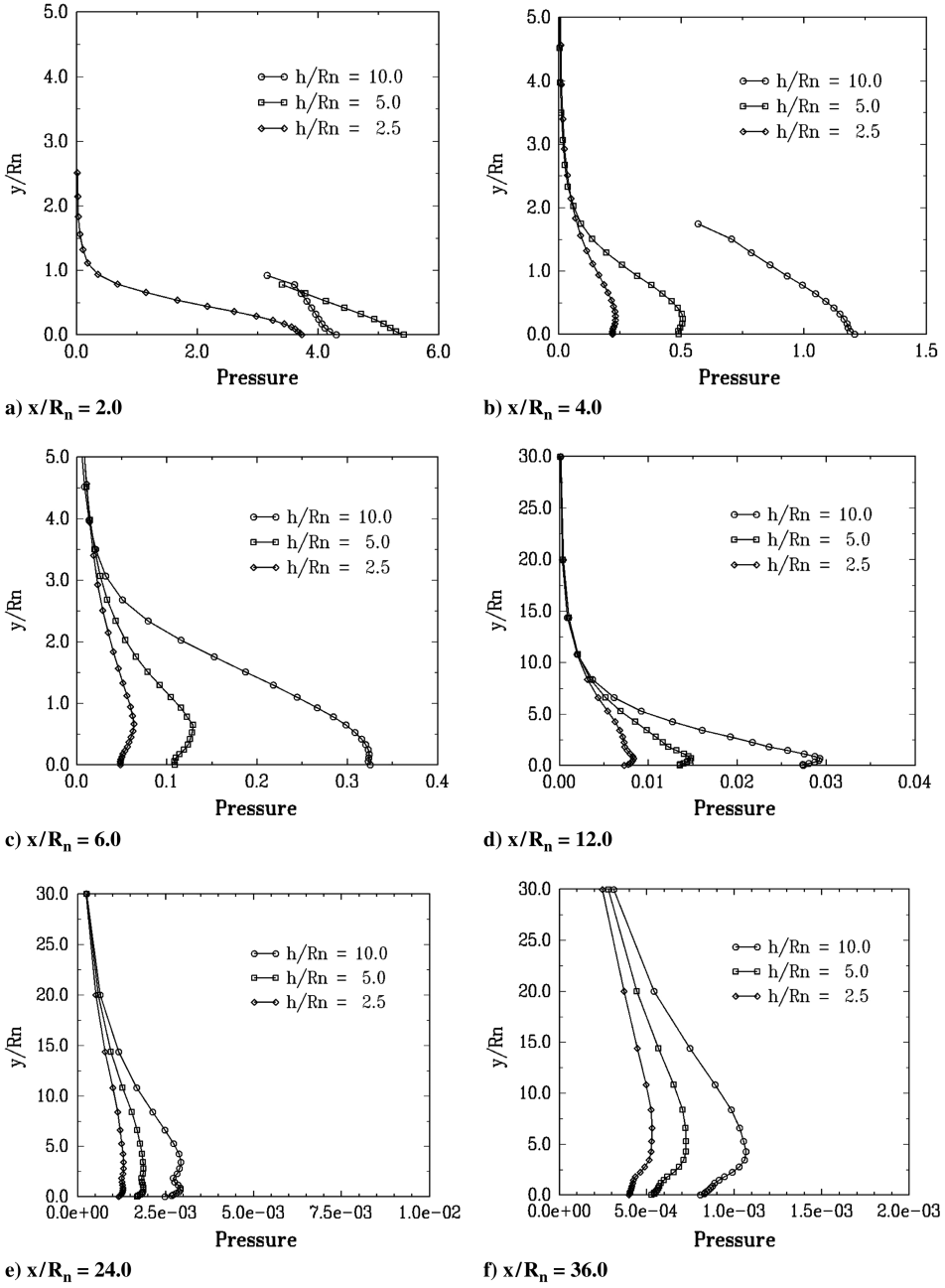

Fig. 17 Pressure profiles.

near-plume continuum through remarkable close-surface gradients that drastically reduce in magnitude and merge into the lunar environment rarefied pressure.

IV. Conclusions

A hybrid continuum-rarefied UFS was used to simulate the effect of hypersonic plume exhaust impingement on a flat surface representing lunar surface. An examination of the accuracy of UFS predictions demonstrated good agreements with plume impingement experiments and theory. A numerical analysis on the details of Apollo lunar lander plume flow characteristics under various impingement heights was then conducted under lunar environment. The axisymmetric UFS predictions were able to smoothly capture the transition of near-plume continuum flow regimes to the plume far-field rarefied lunar conditions. Significant differences in the flow characteristics were revealed with nozzle height variation. The effect of plume expansion on the impingement surface and the gas density in the radial direction was observed to be reduced with the lander descent. In turn, higher surface pressures at the plume center and flow reflection in the vertical direction were observed under lower nozzle heights. The consequent transfer of radial momentum to the surface tangential force was also clearly depicted. Predictions of these mixed continuum-rarefied hypersonic plume flow fields and the corresponding surface forces are directly relevant to the viscous lunar soil erosion mechanism, crater formation and debris transport. Moreover, presence of large or small-scale lunar surface roughness has a direct effect on the soil liberation due to elevated local skin friction. A combined plume-soil interaction and debris transport multiphysics modeling approach is necessary for the analysis of this impact in the lunar environment.

Acknowledgments

This research was supported by the NASA Kennedy Space Center under the Small Business Innovation Research (STTR) program. The authors would like to thank the STTR project technical monitor Philip Metzger (NASA Kennedy Space Center) for his valuable suggestions and continuous guidance on this research. We appreciate expert technical support provided by the lead unified flow solver developer

Vladimir Kolobov (CFD Research Corporation) and Forrest Lumpkin (NASA, Johnson Space Center) for sharing simulation data characterizing the Apollo Lunar Module nozzle flow conditions.

References

[1] Hammock, W. R., Jr., and Currie, E. C., "Apollo Experience Report: Descent Propulsion System," NASA TN-D-7143, 1973.

[2] Land, N. S., and Clark, L. V., "Experimental Investigation of Jet Impingement on Surfaces of Fine Particles in a Vacuum Environment," NASA TN-D-2633, 1965.

[3] Morris, R. V., Score, R., Dardano, C., and Heiken, G., "Handbook of Lunar Soils, Part 1: Apollo 11–15, and Part 2: Apollo 16–17," NASA Johnson Space Center JSC-19069, 1983.

[4] Roberts, L., "Visibility and Dust Erosion During the Lunar Landing" (compilation of recent research related to the Apollo Mission), Center for Aerospace Information Document 19710064822, NASA Langley Research Center, 1963, pp. 155–170.

[5] Lane, J. E., Metzger, P. T., and Immer, C. D., "Lagrangian Trajectory Modeling of Lunar Dust Particles," *Proceedings of Earth and Space 2008, 11th Biennial ASCE Aerospace Division International Conference on Engineering, Construction and Operations in Challenging Environments*, Long Beach, CA, 3–5 March 2008.

[6] Apollo 12 Technical Crew Debriefings (U), 1 Dec. 1969, Manned Spacecraft Center, Houston, TX.

[7] Anderson, D. L., Cunningham, B. E., Dahms, R. G., and Morgan, R. G., "Particle Impact and Optical Property Analysis of the Surfaces of Surveyor 3 Materials," Analysis of Surveyor 3 Material and Photographs Returned by Apollo 12, NASA SP-284, 1972, pp. 76–88.

[8] Immer, C. D., Lane, J. E., Metzger, P. T., and Clements, S., "Apollo Video Photogrammetry Estimation of Plume Impingement Effects," *Proceedings of Earth and Space 2008, 11th Biennial ASCE Aerospace Division International Conference on Engineering, Construction and Operations in Challenging Environments*, Long Beach, CA, 3–5 March 2008.

[9] Carroll, W. F., Davis, R., Goldfine, M., Jacobs, S., Jaffe, L. D., Leger, L., Milwitzky, B., and Nichle, N. L., "Introduction. Analysis of Surveyor 3 Material and Photographs Returned by Apollo 12," NASA SP-284, 1972, pp. 1–8.

[10] Metzger, P. T., Lane, J. E., Immer, C. D., and Clements, S., "Cratering and Blowing Soil by Rocket Engines During Lunar Landings," *Lunar Settlements*, edited by Haym Benaroya, CRC Press, Boca Raton, FL, 2010, pp. 551–576.

[11] Metzger, P. T., Li, X., Immer, C. D., and Lane, J. E., "ISRU Implications of Lunar and Martian Plume Effects," AIAA Paper 2009-1204, 47th AIAA Aerospace Sciences Conference, Orlando, FL, 5–8 Jan. 2009.

[12] Hurt, G. J., Jr., and Lina, L. J., "Blast Effects of Twin Variable-Cant Rocket Nozzles on Visibility During Landing on a Particle-Covered Surface," NASA TN-D-2455, 1964.

[13] Land, N. S., and Scholl, H. F., "Scaled Lunar Module Jet Erosion Experiments," NASA TN D-5051, 1966.

[14] Land, N. S., and Conner, W., "Laboratory Simulation of Lunar Surface Erosion by Rockets," *Institute of Environmental Sciences 13th Annual Technical Meeting Proceedings*, Vol. 1, 1967.

[15] Clark, L. V., "Experimental Investigation of Close Range Rocket Exhaust Impingement on Surfaces in a Vacuum," NASA TN D-5895, 1970.

[16] Clark, L. V., "Effect of Retrorocket Cant Angle on Ground Erosion: A Scaled Viking Study," NASA TM X-2075, 1970.

[17] Carrier, W. D., Costes, N. C., Mitchell, J. K., and Scott, R. F., "Preliminary Geologic Investigation of the Apollo 12 Landing Site: Mechanical Properties of the Lunar Regolith," Apollo 12 Preliminary Science Report, NASA SO-235, 1970, pp. 161–182.

[18] West, G. S., Jr., Wright, J. J., and Euler, H. C., "Space and Planetary Environment Criteria Guidelines for use in Space Vehicle Development: 1977 Revision," NASA TM-78119-REV, 1977.

[19] Roberts, L., "The Interaction of a Rocket Exhaust with the Lunar Surface," *The Fluid Dynamic Aspects of Space Flight*, Vol. 2, pp. 269–290, Proceedings of the AGARD-NATO Specialists' Meeting, Marseille, France, 1964.

[20] Hutton, R. E., "Comparison of Soil Erosion Theory with Scaled LM Jet Erosion Tests," NASA CR-66704, 1968.

[21] Metzger, P. T., Lane, J. E., and Immer, C. D., "Modification of Roberts' Theory For Rocket Exhaust Plumes Eroding Lunar Soil," *Earth and Space 2008, 11th Biennial ASCE Aerospace Division International Conference on Engineering, Construction and Operations in Challenging Environments*, Long Beach, CA, 3–5 March 2008.

[22] Metzger, P. T., Immer, C. D., Donahue, C. M., Vu, B. E., Lata, R. C. III, and Deyo-Svendsen, M., "Jet-Induced Cratering of a Granular Surface with Application to Lunar Spaceports," *Journal of Aerospace Engineering*, Vol. 22, No. 1, 2009, pp. 24–32. doi:10.1061/(ASCE)0893-1321(2009)22:1(24)

[23] Yen, S. M., "Numerical Solution of the Nonlinear Boltzmann Equation for Nonequilibrium Gas Flow Problems," *Annual Review of Fluid Mechanics*, Vol. 16, Jan. 1984, p. 67. doi:10.1146/annurev.fl.16.010184.000435

[24] Bird, G. A., *Molecular Gas Dynamics and the Direct Simulation of Gas Flows*, Clarendon, Oxford, England, U.K., 1994.

[25] Ivanov, M. S., and Gimelstein, S. F., "Computational Hypersonic Rarefied Flows," *Annual Review of Fluid Mechanics*, Vol. 30, Jan. 1998, p. 469. doi:10.1146/annurev.fluid.30.1.469

[26] Garcia, A. L., Bell, J. B., Crutchfield, W. Y., and Alder, B. J., "Adaptive Mesh and Algorithm Refinement Using Direct Simulation Monte Carlo," *Journal of Computational Physics*, Vol. 154, No. 1, 1999, p. 134. doi:10.1006/jcph.1999.6305

[27] Boyd, I. D., "Predicting Breakdown of the Continuum Equations Under Rarefied Flow Conditions," *Rarefied Gas Dynamics: 23rd International Symposium, AIP Conference Proceedings* edited by A. D. Ketsdever and E. P. Munz, Vol. 663, 2003, pp. 899–906.

[28] Beylich, A. E., "Solving the Kinetic Equation for all Knudsen Numbers," *Physics of Fluids*, Vol. 12, No. 2, 2000, p. 444. doi:10.1063/1.870322

[29] Wang, W. L., and Boyd, I. D., "Hybrid DSMC-CFD Simulations of Hypersonic Flow over Sharp and Blunted Bodies," AIAA Paper 2003-3644, 2003.

[30] Wu, J.-S., Lian, Y.-Y., Cheng, C., Koomullil, R., and Tseng, K.-C., "Development and Verification of a Coupled DSMC-NS Scheme Using Unstructured Mesh," *Journal of Computational Physics*, Vol. 219, No. 2, 2006, pp. 579–607. doi:10.1016/j.jcp.2006.04.013

[31] Lumpkin, F., Marichalar, J., and Piplica, A., "Plume Impingement to the Lunar Surface: A Challenging Problem for DSMC," Direct Simulation Monte Carlo: Theory, Methods, and Application, Santa Fe, NM, 30 Sept.–3 Oct. 2007.

[32] Carlson, H. A., Roveda, R., Boyd, I. D., and Candler, G. V., "A Hybrid CFD-DSMC Method of Modeling Continuum-Rarefied Flows," AIAA Paper 2004-1180, 2004.

[33] Kolobov, V. I., Yang, H. Q., Bayyuk, S. A., Aristov, V. V., Frolova, A. A., and Zabelok, S. A., "Unified Methods for Continuum and Rarefied Flows," AIAA Paper 2004-1177, 2004.

[34] Popinet, S., "Gerris: A Tree-Based Adaptive Solver for the Incompressible Euler Equations in Complex Geometries," *Journal of Computational Physics*, Vol. 190, No. 2, 2003, pp. 572–600. doi:10.1016/S0021-9991(03)00298-5

[35] Kolobov, V. I., Bayuuk, S. A., Arslanbekov, R. R., Aristov, V. V., and Zabelok, S. A., "Construction of a Unified Continuum/Kinetic Solver for Aerodynamic Problems," *Journal of Spacecraft and Rockets*, Vol. 42, No. 4, 2005, pp. 598–606. doi:10.2514/1.10468

[36] Kolobov, V. I., Arslanbekov, R. R., Aristov, V. V., Frolova, A. A., and Zabelok, S. A., "Unified Flow Solver for Rarefied and Continuum Flows with Adaptive Mesh and Algorithm Refinement," *Journal of Computational Physics*, Vol. 223, No. 2, 2007, pp. 589–608. doi:10.1016/j.jcp.2006.09.021

[37] Pullin, D. I., "Direct Simulation Methods for Compressible Inviscid Ideal Gas Flow," *Journal of Computational Physics*, Vol. 34, No. 2, 1980, p. 231. doi:10.1016/0021-9991(80)90107-2

[38] Ohsawa, T., and Ohwada, T., "Deterministic Hybrid Computation of Rarefied Gas Flows," *Rarefied Gas Dynamics: 23rd International Symposium, AIP Conference Proceedings*, edited by A. D. Ketsdever and E. P. Munz, Vol. 663, 2003, pp. 931–938.

[39] Cercignani, C., *The Boltzmann Equation and its Applications*, Springer–Verlag, New York, 1988.

[40] Josyula, E., Arslanbekov, R. R., Kolobov, V. I., and Gimelshein, S. F., "Evaluation of Kinetic/Continuum Solver for Hypersonic Nozzle-Plume Flow," *Journal of Spacecraft and Rockets*, Vol. 45, No. 4, 2008, pp. 665–676. doi:10.2514/1.35431

[41] Roberts, L., "The Action of a Hypersonic Jet on a Dust Layer," Institute of Aerospace Sciences Paper 63-50, Institute of Aerospace Sciences 31st Annual Meeting, New York, 21–23 Jan. 1963.

I. Boyd
Associate Editor